Aerosol Indirect Effect Studies at Southern Great Plains during the May 2003 Intensive Operations Period

[1]Graham Feingold, [2]Reinhard Furrer, [3]Peter Pilewskie,
[4]Lorraine A. Remer, [5]Qilong Min and [6]Haflidi Jonsson

In Press

[1]NOAA, Environmental Technology Laboratory 325 Broadway, Boulder, Colorado 80305

[2]National Center for Atmospheric Research, Boulder, Colorado 80307

[3]University of Colorado, Boulder, Colorado 80303

[4]NASA/ Goddard Space Flight Center, Greenbelt Maryland

[5]ASRC, SUNY Albany

[6] Center for Interdisciplinary Remotely-Piloted Aircraft Studies (CIRPAS)
Naval Postgraduate School, Monterey, California

In Press

Corresponding Author Address:
Graham Feingold
NOAA Environmental Technology Laboratory
325 Broadway, Boulder CO 80305, USA
Tel: (303) 497-3098
E-mail: graham.feingold@noaa.gov

Abstract. During May 2003 the Department of Energy's Atmospheric Radiation Measurement Program conducted an Intensive Operations Period (IOP) to measure the radiative effects of aerosol and clouds. A suite of both in-situ and remote sensing measurements were available to measure aerosol and cloud parameters. This paper has three main goals: First, it focuses on comparison between in-situ retrievals of the radiatively important drop effective radius r_e, and various satellite, airborne, and surface remote sensing retrievals of the same parameter. On May 17 2003 there was a fortuitous, near-simultaneous sampling of a stratus cloud by five different methods. The retrievals of r_e agree with one another to within $\sim 20\%$, which is approximately the error estimate for most methods. Second, a methodology for deriving a best estimate of r_e from these different instruments, with their different physical properties and sampling volumes, is proposed and applied to the May 17 event. Third, the paper examines the response of r_e to changes in aerosol on three days during the experiment and examines the consistency of remote sensing and in-situ measurements of the effect of aerosol on r_e. It is shown that in spite of the generally good agreement in derived r_e, the magnitude of the response of r_e to changes in aerosol is quite sensitive to the method of retrieving r_e, and to the aerosol proxy for cloud condensation nuclei. Non-physical responses are sometimes noted and it is suggested that further work needs to be done to refine these techniques.

1

1. Introduction

The effect of suspended atmospheric particles, or aerosol, on the microphysics of clouds has for decades been the subject of intense scrutiny. *Twomey* [1974] proposed that for a constant amount of condensed water, an increase in the number of cloud condensation nuclei (CCN) will generate a cloud that consists of smaller drops and reflects more energy to space. This process is commonly referred to as the "first aerosol indirect effect". The ensuing decades have seen intensive field campaigns [e.g., *Leaitch et al.,* 1996; *Brenguier et al.,* 2000; *Ramanathan et al.,* 2001], particularly in ship tracks, where aerosol influences on stratocumulus clouds are distinctly visible [*Durkee et al.,* 2000]. In recent years, satellite remote sensors have been employed to provide a regional [*Kaufman and Nakajima,* 1993; *Rosenfeld and Lensky,* 1998] and even global view [*Han et al.,* 1998; *Nakajima et al.,* 2001; *Bréon et al.,* 2002] of aerosol effects on clouds. More recently still, surface-based remote sensors have examined aerosol effects on clouds based on high temporal/spatial resolution data [*Feingold et al.,* 2003] and longer term analyses [*Kim et al.,* 2003; *Garrett et al.,* 2004] at a few select sites.

While there is ample evidence that an increase in aerosol tends to decrease cloud drop size and increase cloud reflectance, many questions remain concerning the degree to which this occurs, the most important controlling parameters, and the measurement requirements for these parameters. For example, although the concept of the first indirect effect posed by *Twomey* [1974] clearly states that the comparison be made between clouds having the same liquid water content, many studies have ignored this requirement. Therefore, it is unclear whether drop sizes are smaller because of higher CCN concentrations or because of lower condensed water [*Schwartz et al.,* 2002]. Other important questions include the relative importance of cloud dynamics (particularly updraft velocity), aerosol composition, and aerosol size distribution [*Feingold,* 2003]. Although it is clear that aerosol effects on clouds extend to cloud lifetime, precipitation [*Warner,* 1968; *Albrecht,* 1989], and cloud dynamics,

an understanding of the magnitude of the first indirect effect is in and of itself a worthy goal.

Because field campaigns are limited in scope and duration, it is desirable to evaluate the first indirect effect in a continuous fashion using remote sensing. However, it is important to establish whether these remote sensors can measure the required parameters, and whether they can do so with sufficient sensitivity. Aerosol optical depth (AOD), a parameter readily measured by satellites and surface networks such as the Aerosol Robotic Network (AERONET) [*Holben et al.,* 1998], is often used to represent CCN [*Kaufman and Nakajima,* 1993]; however, *Feingold* [2003] showed that AOD may not always be a good proxy for the CCN affecting the cloud. There are two reasons: first, the path-integrated nature of the measurement means that variations in the aerosol entering the cloud may not be captured by the AOD, and second, because the existence of variability in the aerosol size distribution and composition will reduce the overall response of drop size to AOD [*Feingold* , 2003]. *Nakajima et al.,* [2001] proposed the use of an "aerosol index" (the product of the AOD and Ångström exponent) and showed that a higher sensitivity of aerosol effects on cloud can be obtained. In spite of this inherent sensitivity associated with the aerosol index, *Bréon et al.* [2002] found a much weaker response of cloud drop size to changes in the aerosol index than expected from theory. The reasons could be rooted in variability in cloud water and aerosol size and composition [*Feingold,* 2003], or perhaps due to biases in the types of clouds observed [*Rosenfeld and Feingold,* 2003].

The motivation of this paper is threefold: (i) to establish whether there is agreement between remotely sensed measures of cloud drop effective radius r_e $(= \langle r^3 \rangle / \langle r^2 \rangle$, where $\langle r^n \rangle$ is the nth moment of the drop size distribution) in a relatively homogeneous stratus cloud that covered the surface measurement site at the Southern Great Plains site in Oklahoma on May 17 2003; (ii) to develop a rigorous mathematical methodology for retrieving a best estimate of drop size from a variety of different instruments with different temporal resolutions, sampling volumes, and physical bases

for measurement; and (iii) to establish whether a measure of the first indirect effect derived from different drop-size retrievals and different CCN proxies yields consistent results. This exercise is a small step in establishing the extent to which remote sensors can be relied upon to quantify the first aerosol indirect effect. We begin with a brief description of the instruments and retrieval techniques used by the various in-situ and remote sensors. We then show results pertaining to the three goals and conclude with discussion and a summary.

2. Instrumentation

The instruments used in this study are the following:

 (i) A ground-based Microwave Radiometer (MWR) [*Liljegren,* 1999];

 (ii) A ground-based Multi-Filter Rotating Shadowband Radiometer (MFRSR) [*Harrison and Michalsky,* 1994];

(iii) A ground-based Millimeter Cloud Radar (MMCR) [*Moran et al.,* 1997];

(iv) An airborne Solar Spectral Flux Radiometer (SSFR) [*Pilewskie et al.,* 2003];

 (v) The satellite-based Moderate-Resolution Imaging Spectroradiometer (MODIS) [*Guenther et al.,* 2002];

(vi) The Cloud, Aerosol, and Precipitation Spectrometer (CAPS) in-situ airborne probe [*Baumgardner et al.,* 2001].

Below we provide a brief description of the instruments and Table 1 summarizes some of their sampling characteristics.

(i) MWR

The Microwave Radiometer measures time series of column-integrated water vapor and liquid water based on the microwave emissions of atmospheric vapor and liquid water molecules at specific frequencies. By measuring water vapor emissions at 23.8

GHz and liquid water emissions at 31.4 GHz, both water vapor and liquid water can be separated. Typical uncertainties in the column-integrated liquid water (LWP) are 25–30 g m^{-2}.

(ii) MFRSR

The MFRSR measures spectral direct normal, diffuse horizontal, and total horizontal solar irradiances at nominal wavelengths of 415, 500, 615, 673, 870, and 940 nm every 20 seconds. The MFRSR allows accurate determination of atmospheric transmittances without requiring absolute calibration because it measures both total horizontal irradiance and direct-normal irradiance using the same detectors by a blocking technique. Consequently, Langley regression of the direct-normal irradiance taken on stable clear days can be used to extrapolate the instrument's response to the top-of-the-atmosphere, and this calibration can then be applied to the total horizontal irradiance on overcast periods. Transmittances are calculated subsequently under cloudy conditions as the ratio of the uncalibrated MFRSR signal to the extrapolated top-of-the-atmosphere value.

Min and Harrison [1996a] and *Min et al.* [2004] have developed a family of inversion methods to infer cloud optical properties from MFRSR combined with MWR. As is standard, the cloud radiative properties are parameterized in terms of a cloud averaged drop effective radius r_e, and total liquid water path, LWP, based on Mie theory [*Hu and Stamnes,* 1993]. Using total horizontal transmittance at 415 nm, together with LWP, one can simultaneously retrieve cloud optical depth and r_e through the use of a nonlinear least squares minimization in conjunction with an adjoint method of radiative transfer [*Min and Harrison,* 1996b].

Based on extensive comparison with in-situ measurements [*Min and Harrison,* 1998; *Barnard et al.,* 2001], it is estimated that for single-layer, warm clouds, the MFRSR-derived r_e agree to within 5.5% with in-situ measurements. Sensitivity studies also illustrate that for this case, a 13% uncertainty in observed LWP (20 g m^{-2}) results in a 1.5% difference in retrieved cloud optical depth, and an average uncertainty in r_e of

12.7%. The uncertainty of the LWP measured by the MWR is the major contributor to the uncertainty in retrieved r_e [*Min et al.*, 2003].

The instantaneous effective "footprint" of a cloud sampled by the MFRSR is a circle of radius ~ 1 km (or about 3 times the "radiative smoothing scale"). The data are recorded at 5 min resolution which, at an advective velocity scale of 3 m s^{-1} for the day in question, translates to a footprint with a radius equal to 900 m, i.e., roughly the size of the instantaneous footprint *Min et al.* [2001]. In general, the footprint depends on the cloud height.

(iii) MMCR

The Millimeter Cloud Radar is a highly sensitive, vertically pointing, Doppler radar operating at a wavelength of 8.6 mm, designed to measure clouds. The MMCR has a 0.19° beam width and a 45 m range gate. Its velocity resolution is 0.1 m s^{-1} . At an altitude of 1200 m, the sample volume is ~ 700 m^3.

The MMCR drop-size retrieval was first published by *Frisch et al.* [1995] and later updated by *Frisch et al.* [2002]. The basic methodology consists of combining a radar profile of reflectivity Z with a microwave radiometer constraint on path-integrated liquid water content (LWP) to produce a system of $N + 1$ measurements at N range gates. Using a drop-size distribution model and an assumption of a fixed spectral dispersion (σ = the natural log of the geometric standard deviation = constant), the system of equations is solved to produce a profile of r_e and a constant (with height) drop concentration N_d. It is the only one of the remote sensing techniques that produces a drop-size profile. Because of the very high sensitivity of reflectivity to drop size, drizzling clouds are avoided by only considering conditions for which Z < -17 dBZ. The existence of even small concentrations of large drizzle drops could produce significant reflectivity signal and bias drop-size retrievals.

Frisch et al. [2002] showed that more robust retrievals can be obtained by further requiring N_d to be a fixed constant, with minimal effect on accuracy of the retrieval

of r_e because $r_e \propto (Z/N_d)^{1/6}$. Typical values for the appropriate aerosol conditions can be assumed. The *Frisch et al.* [2002] algorithm is adopted here, with further scaling of the retrieved r_e profile such that the retrieved LWP is the same as that measured by MWR. The error in r_e can be shown [*Frisch et al.*, 2002] to be:

$$\frac{\Delta r_e(z)}{r_e(z)} \sim \pm \left[\left(\frac{\Delta Z}{6Z(z)} \right)^2 + (4\sigma \Delta \sigma)^2 + \left(\frac{\Delta \text{LWP}}{3\text{LWP}} \right)^2 \right]^{1/2}. \tag{1}$$

With typical errors in Z of 1 dBZ, σ of 0.1, and LWP of 30 g m^{-2}, respectively, the error in r_e is $\sim 16\%$.

(iv) SSFR

During the IOP the SSFR was integrated onto the CIRPAS Twin Otter aircraft to measure upwelling- and downwelling-solar spectral irradiance. The SSFR comprises a pair of identical spectrometers that measure in the spectral region between 300 nm and 1700 nm. Pairs of Zeiss Monolithic Miniature Spectrometer Modules (MMS 1 and MMS NIR) are used for simultaneous zenith and nadir viewing. The MMS-1 modules are temperature stabilized at 27° C $\pm$ 0.3° C and the MMS-NIR are thermoelectrically cooled to 0° C. Spectral resolution is 9 nm for the MMS-1 and 12 nm for the MMS-NIR. In-flight integration time for each of the spectrometers is nominally 100 ms. The spectral sampling rate is approximately 1 Hz. The SSFR is calibrated for wavelength response, angular response, and absolute spectral power. Estimated RMS uncertainty across the spectrum is 3% to 5% for the SSFR spectral range between 350 and 1700 nm; precision is between 0.1% and 0.3%.

The spectral irradiance reflected at cloud top was normalized by the downwelling spectral irradiance to determine the spectral albedo of the cloud. These data contain the necessary information to infer r_e and cloud optical depth τ_d, the product of which is proportional to LWP. The retrieval procedure determines the $(r_e; \tau_d)$ pair from libraries of computed cloud spectral albedo over a broad range in r_e and τ_d. The radiative transfer code has been described in *Bergstrom et al.* [2003]. A search

algorithm using as few as five wavelengths and similar to that of *Twomey and Cocks* [1989], is used to determine the closest match to the measured spectral albedo. The measurement-model residuals for most cases are found to be less than 5% and close to the uncertainty in the measurements.

For hemispheric irradiance measurements, and assuming an isotropic radiation field, half of the measured signal is derived from within 45° of normal incidence. Therefore, we define the footprint of SSFR to be a circle of radius equal to the distance from the aircraft to cloud, which for the case under discussion is 2700 m.

(v) MODIS

The retrieval of r_e and τ_d is made from simultaneous measurements in one water-absorbing band (1.6, 2.1 or 3.7 μm) and one nonabsorbing band (0.65, 0.86 or 1.2 μm). The cloud must first be identified as either a water cloud or an ice cloud. Then the measured reflectances are matched to a lookup table of calculated reflectances, which have been calculated separately for either water or ice. The resulting product is produced at 1 km resolution for high elevation angles but is somewhat coarser for lower elevation angles. The nonabsorbing band is chosen to minimize the effect of surface reflectance in the retrieval, and only one of those bands is used in each retrieval. However, the retrieval is performed separately for each of the three water-absorbing bands and all three results are reported [*Platnick et al.,* 2003]. The three wavelengths provide limited information on the vertical distribution of the droplet effective radius, but all are weighted towards the cloud top. Retrieval uncertainty is dependent on many factors including τ_d, geometry of the observation and surface type and reflectance. Typical uncertainties range from 5 to 10% for homogeneous unbroken clouds.

(vi) CAPS

The CAPS (Cloud-Aerosol-Precipitation-Spectrometer) probe (Droplet Measurement Technologies, Boulder, Colorado) is an airborne in-situ device consisting of a

combination of forward and backscatter sensors covering the diameter range from ~ 0.8 to 50 μm and an occultation sensor that sizes drops in the 25 – 1500 μm diameter range. The scatter probe was operated with 20-channel resolution, where channel boundaries were set at equal logarithmic pulse height intervals. As a result, resolution was high in the lower size bins (about 0.3 μm per bin) and lower in the higher bins (approximately 5 μm per bin). The CAPS probe flew on the CIRPAS Twin Otter aircraft and sampled at a rate of 1 Hz, which at the aircraft speed of $\sim$ 50 m s^{-1} corresponds to a length scale of 50 m. The sample area is 120 μm $\times$ 1.1 mm, resulting in an approximate sampling volume of ~ 6.6 cm^3. Note that although this type of measurement provides what is often regarded as our most accurate measure of drop size, the sample volume is significantly smaller than those of the remote sensors.

The pulse height distributions measured by the forward scatter section of the CAPS probe were inverted to particle size distributions based on calibrations and theoretical estimations of the probe's response. Considerable uncertainties are inherent in this inversion process, particularly in the range of sizes that are affected by Mie resonances. In this size range (between 1 and 10 μm diameter), water droplets having several different diameters may generate identical scattered light pulses. There is therefore no certain link from a measured pulse to a particular diameter. The range of possible diameters varies by a factor of 2. For particles larger than 10 μm in diameter, the Mie oscillations in the probe's response dampen considerably, and the uncertainty in the inverted values shrinks to approximately 30%.

Uncertainty in particle concentration measured by the CAPS scatter probe is dominated by an inability to accurately measure the active area of the laser, which along with the true airspeed of the airplane determines the probe's viewing volume. Instead, values furnished by the manufacturer must be used, that are mainly based on design and manufacturing tolerances. Confidence in the view volume estimates may however be attained by comparing particle size distributions obtained in dry air by the CAPS probe with those simultaneously measured by the overlapping channels

in the PCASP (Passive Cavity Aerosol Spectrometer Probe), where concentration determination rests on a sample flow measurement. Further comparisons with other independent measurements, such as liquid water content, further bolster confidence. A quantitative estimate of uncertainty in view volume (concentration) is not ventured here, but comparisons as described above have yielded what may be characterized as good agreement and consistency. Considering all these effects we estimate that the accuracy in retrieved r_e is $15 - 20\%$.

We note that the remote retrievals of r_e for the most part use quite different approaches (Table 1). The two downward looking instruments, SSFR and MODIS, use conceptually similar solar spectrometer methods, neither of which relies on an independent measure of LWP. They both directly measure r_e, i.e., $\langle r^3 \rangle / \langle r^2 \rangle$. The two surface-based remote measurements, MFRSR and MMCR, are quite different in that they use passive, visible radiometry ($\propto \langle r^2 \rangle$) and active, microwave radar ($\propto \langle r^6 \rangle$), respectively. Both methods rely on an independent measure of LWP ($\propto \langle r^3 \rangle$) by MWR. The radar retrieval of r_e by MMCR is the only method that can provide profiles of r_e, both day and night, but it is also the most sensitive to drizzle. All other methods yield either cloud-top weighted r_e (SSFR and MODIS), or cloud averaged r_e (MFRSR), during daylight hours when the solar elevation angle is sufficiently high.

3. Results

3.1. General

The conditions on May 17 2003 were characterized by light northerly flow of about 3 m s^{-1} (in the boundary layer) following passage of a low pressure system. Figures 1 and 2 provide Aqua satellite, surface radar (MMCR), and surface microwave radiometer (MWR) views of the clouds. Cloud cover was relatively homogeneous following a period of light drizzle that ended at about 17:00 UTC, with a tendency to thin as daytime heating progressed. Our analysis is restricted to the period after 17:00 UTC. (Henceforth all references to time are in hours UTC.) LWPs ranged from ~ 200 g m^{-2} to 10 g m^{-2} (Figure 2b) and decreased steadily over the analysis period.

This case provided a useful target cloud for comparing the various retrieval methods because (a) the relative homogeneity of the cloud provides higher confidence in the optical remote sensing retrievals of r_e produced by MFRSR and SSFR, and (b) radar reflectivities were less than -20 dBZ and therefore the clouds were unlikely to have contained drizzle drops.

The CIRPAS Twin Otter aircraft took off from the Ponca City, Oklahoma airport at approximately 18:48 h. Soon after (19:01 h) it penetrated the cloud (Figure 3) which was characterized by liquid water content (LWC) of up to 0.3 g m^{-3}, N_d of 400 – 500 cm^{-3} and r_e of 5 – 6 μm. At the time of penetration, the aircraft was 30 km from the SGP site. At 19:48 h, the aircraft flew over the SGP site (latitude +36.605, longitude −97.489) at an altitude of 4200 m, or about 2700 m above the cloud top. The downward looking SSFR retrieved an r_e at this time of ~ 5 μm (Figure 4). Time series plots of the MMCR and MFRSR r_e are shown in Figure 5 and indicate r_e of ~ 6 μm at the time of the overflight.

The Aqua satellite carrying MODIS passed over the site at 18:45 h with a peak elevation angle of 27°. The MODIS-retrieved r_e is depicted in Figure 6 as a spatial histogram; The size of each box is approximately 2 km (in the N-S direction) × 4.8 km (in the E-W direction) owing to the relatively low elevation angle.

We note good consistency between all measures of r_e with differences on the order of 20%, i.e., at the level of uncertainty associated with the retrievals.

3.2. Drop-size Retrieval Comparisons: A Methodology for Comparing Retrievals by Instruments with Different Sampling Characteristics

The different methodologies for retrieving r_e (e.g., passive radiometry vs. active radar), and different viewing angles, sample volumes, and averaging times associated with the various instruments present an interesting case when attempting to derive a best estimate of drop size. In the following section, we describe a methodology for doing so that is based on the method of optimal estimation. Its application should

be considered illustrative and exploratory as various assumptions and simplifications have been applied. It is intended to lay the groundwork and approach for more extensive comparisons and retrievals in future work.

3.2.1. Combining Different Scales and Uncertainties

In keeping with our notation, we denote the cloud drop effective radius at height above ground level h, time t and horizontal location $\mathbf{s}$ with $r_e(h, t, \mathbf{s})$. For the present approach, we assume that for sufficiently small spatial and temporal scales, r_e does not change systematically, either horizontally or with time. We use a first-order approximation for the functional dependence of r_e on h based on an adiabatic cloud with fixed N_d,

$$r_e(h, t, \mathbf{s}) = \theta_1 + \theta_2 h^{1/3} + \mathcal{Z}, \tag{2}$$

where $\mathcal{Z}$ is a Gaussian process modeling the remaining spatial and temporal variability of the cloud, i.e., the small-scale cloud structure. The mean of the process $\mathcal{Z}$ is zero, but the variance of $\mathcal{Z}$ may change in a complex manner. Note that the model is linear in the parameters of interest, i.e., the intercept θ_1 and the slope θ_2. The objective is to combine the different types of retrievals by accounting for the sample volumes, averaging times, and retrieval uncertainties to derive estimates for θ_1 and θ_2.

The retrievals from the instruments having the smallest sampling volume are considered "point" retrievals; the others are integrated and/or weighted over some spatial domain. For example, the MODIS data represent the quantity

$$\frac{1}{|\mathcal{H}|} \frac{1}{|\mathcal{S}|} \frac{1}{|\mathcal{T}|} \int_{\mathcal{H}} \int_{\mathcal{S}} \int_{\mathcal{T}} r_e(h, t, s) \, \omega_{\text{MODIS}}(h, t, \mathbf{s}) dt \, d\mathbf{s} \, dh \tag{3}$$

where $\mathcal{H}$, $\mathcal{S}$, and $\mathcal{T}$ represent the cloud column, footprint region, and time frame, and ω_{MODIS} is a weighting function describing the contribution to reflectance as a function of height in the cloud. The form of these weighting functions is closely tied to the vertical structure of the cloud, and to the solar zenith and viewing angles [*Platnick* 2000]. In the current example we simplify the choice of weighting to an exponential function, which is only strictly true if penetration depth is defined as the level at

which photons encounter their first scattering. To obtain a sense of the sensitivity to weighting function, we will apply two different exponential forms. The choice of weighting functions for MODIS and the other instruments is discussed further in the Appendix.

Similar relationships to (3) hold for the other retrievals. A major advantage of the linearity assumption (2) is that integrals as in (3) are still linear in θ_1 and θ_2.

The key assumption in the statistical model is that the retrievals are unbiased values of the true (integrated) r_e, i.e., that there are no systematic errors in the retrievals (e.g., possible biases due to broken clouds). However, we allow for zero mean symmetrical retrieval errors of different magnitudes for each of the instruments. For simplicity, all errors are assumed to be Gaussian and uncorrelated between instruments. For each instrument we allow for correlation within height, time and horizontal position. Then, stacking all the retrievals into a single vector, say $\mathbf{R}$, we can write

$$\mathbf{R} = \mathbf{M}\,\boldsymbol{\theta} + \boldsymbol{\epsilon}, \qquad \mathrm{Cov}(\boldsymbol{\epsilon}) = \boldsymbol{\Sigma}, \tag{4}$$

where $\mathbf{M}$ is the so-called design matrix, $\boldsymbol{\theta} = (\theta_1, \theta_2)^T$, and the random vector $\boldsymbol{\epsilon}$ consists of the retrieval errors and the process $\mathcal{Z}$. The first column of the matrix $\mathbf{M}$ contains ones; the entries of the second column depend on the corresponding retrievals. For "point" retrievals at height h the corresponding entry is $h^{1/3}$, whereas for MODIS data it is

$$\frac{1}{|\mathcal{H}|} \int_{\mathcal{H}} h^{1/3} \omega_{\mathrm{MODIS}}(h) dh, \tag{5}$$

provided the weighting function depends on height only, and so on (see also Appendix).

Equation (4) represents a linear regression model with correlated errors. The parameter of interest $\boldsymbol{\theta}$ can be estimated with a generalized least squares approach, i.e., by minimizing a cost function consisting of the sum of weighted squared errors. The solution to this minimization problem is

$$\hat{\boldsymbol{\theta}} = (\mathbf{M}^T\,\boldsymbol{\Sigma}^{-1}\,\mathbf{M})^{-1}\,\mathbf{M}^T\,\boldsymbol{\Sigma}^{-1}\,\mathbf{R}, \tag{6}$$

13

$$\text{Cov}(\hat{\boldsymbol{\theta}}) = (\mathbf{M}^T \, \boldsymbol{\Sigma}^{-1} \mathbf{M})^{-1}, \tag{7}$$

from which we can derive confidence intervals or statistical hypothesis tests for the parameters θ_1 and θ_2.

The statistical model relies on a few reasonable assumptions. First, we assume a simple linear relationship between r_e and the height function $h^{1/3}$. If we impose $\theta_2 = 0$, then the estimate of θ_1 gives us the best overall estimate of the drop size. Further, it is possible to change the height function to any arbitrary function of h, parameterized by a parameter vector $\boldsymbol{\theta}$, although we see no reason to add complexity of this kind for the illustrative example presented here. Second, we impose a Gaussian structure on $\mathcal{Z}$ and the retrieval errors, which is reasonable based on the analysis of the data of May 17. However, this assumption could be relaxed to other zero-mean variates, for which the solution given in Equation (6) is still the best linear unbiased estimator. In this case, however, the associated tests and confidence intervals would need some adjustment.

3.2.2. Data and Parameter Selection

We are in the fortunate position of having a great deal of data (on the order of 10,000) and the model has very few parameters of interest (two in our case). For the statistical analysis, we cannot use all the retrievals during the operational period. We will only consider data within a spatial and temporal window in which we assume that the cloud has no systematic variability. The in-situ CAPS measurements were taken 30 km from the SGP site, a distance too large to assume cloud homogeneity. This can be seen by considering that the advective velocity scale of 3 m s^{-1} and the distance of 30 km correspond to a characteristic time scale of nearly 3 h. Over this period of time, Figure 2 indicates significant changes in cloud structure. Physical examination of the clouds at each location suggests a different structure, for example, the cloud top is roughly 200 m lower at the SGP site compared to the CAPS cloud penetration location. Furthermore, the SSFR data are highly correlated in time and the inclusion of many retrievals does not increase the information content compared

to very few uncorrelated retrievals.

As in any dynamical system, there is no absolute criterion for homogeneity or stationarity, and it is a nontrivial task to determine the spatial and temporal window within which we can assume "local" stationarity. There is no universal tool to perform the data selection and this part requires intervention by the scientist.

The model has several additional (nuisance) parameters, such as the error correlation structure and the weighting functions. Most of these parameters are not available and only rough bounds are known. However, the model presented above does allow parameter checking. After fitting a linear model, it is possible to use statistical inference to verify the model assumptions.

3.2.3. Numerical Example

The aforementioned discussion leads to the following data selection:

- MFRSR: 6 retrievals over a 30-minute period between 19:20 h and 19:50 h;

- MMCR: 91 column retrievals between 19:20 h and 19:50 h (the lowest and uppermost radar range gates have been eliminated, resulting in a total of 688 values);

- SSFR: 3 retrievals between 19:47 h and 19:49 h. We thin the data to eliminate the high correlation intrinsic to the data;

- MODIS: 3×3 pixels of size 2 km×4.8 km, centered at the SGP site at 18:45 h. Although the MODIS data were measured 35 min before the analysis window they exhibit similar optical depths to those measured during the 30 minute period. They exhibit no spatial correlation (Figure 6) and are therefore deemed suitable for use in the analysis.

This selection essentially covers a spatial window of approximately 6 km or 35 minutes to include the SSFR and MODIS data.

For the selected data points, the design matrix $\mathbf{M}$ and the covariance matrix $\boldsymbol{\Sigma}$ have to be specified, as discussed in detail in the Appendix. Based on Figure 2a, it is assumed that the cloud extends from $h = 675$ m to 1350 m. We assume that the weighting function for MFRSR (transmission measurement) is constant throughout the cloud column, which is a reasonable first-order approximation for the current exercise [*Platnick* 2000]. For both SSFR and MODIS, we use an exponential weighting related to the penetration depth. In reality SSFR and MODIS weighting functions differ and, as discussed earlier, are not strictly exponential. This weighting is therefore varied to explore sensitivity of the retrieved r_e profile. For the covariance matrix, we need to determine the correlation structure of $\mathscr{Z}$ and specify the retrieval errors. However, separating the retrieval error from other small-scale structures is a nontrivial problem [*Cressie*, 1993, pages 112ff]; therefore, we directly specify the covariance matrix. For the MMCR data we modeled temporal and spatial correlation not extending over more than 200 m, the typical size of the large eddies; however the CAPS data would even support smaller correlation lengths. Further, it is assumed that the variation of $\mathscr{Z}$ is much smaller than the retrieval errors, a fact confirmed after model fitting. The other retrievals are assumed to be independent, as indicated by the data.

Applying the above methodology and parameters (exponential weighting function having 1/17 m decay) the estimated values for the intercept θ_1 and the slope θ_2 are 2.31 and 0.38 with 95% confidence intervals [2.31 ± 1.17] and [0.38 ± 0.12] respectively. For cloud bottom and cloud top r_e is estimated to be 5.57μm and 6.54μm respectively. Note that both parameters are statistically significantly different from zero. The percentage of variance explained by the linear model (R^2 or coefficient of determination) is 97.6%. When we decrease the decay rate of the weighting function from 1/17 m to 1/340 m, the 95% confidence intervals of the parameters change to [4.45 ± 1.58] and [0.17 ± 0.16] respectively. Figure 7 summarizes the selected data and the best estimate(s) for the example presented. We note the effect of the choice of the weighting function on r_e ; the slower decaying exponential tends to create less vertical variation in r_e by allowing the influence of MODIS and SSFR data to penetrate to

deeper levels in the cloud. These differences are expected to be somewhat smaller for more reasonable variability in weighting function. Nevertheless, we stress the importance of appropriate attention to weighting functions for all instruments when retrievals of this kind are applied (see further discussion in the Appendix).

To illustrate the importance of taking into account the covariance matrix $\boldsymbol{\Sigma}$, we also calculate the estimate without using weighted squared errors, as well as the global mean. Since the MODIS retrievals have a small retrieval error, they receive larger weights than SSFR and MFRSR, which explains the difference between the weighted and unweighted fits. For a small decay rate of the weighting function the MODIS data induce a leveraging effect. The MFRSR retrievals and the small r_e retrievals of the MMCR higher up in the cloud induce large residuals that do not exhibit a perfect Gaussian distribution.

4. Aerosol Effects on Clouds

The third part of this paper focuses on the first aerosol indirect effect and measurement thereof using surface-based remote sensors. Although the first indirect effect is primarily a question of changes in cloud reflectance due to changes in aerosol, at the heart of this problem is the relationship between cloud drop number concentration N_d and aerosol number concentration N_a, or, for clouds of equal LWC, the relationship between r_e and N_a. Assuming sub-cloud lidar extinction to be a proxy for CCN, *Feingold et al.* [2003] used MMCR and MWR to retrieve r_e and examined changes in r_e as a function of changes in sub-cloud lidar extinction. The method can provide a short time scale (~ 20 s) view of cloud response to changes in the aerosol entering the cloud base. Using the radar's Doppler capability, one can conditionally sample the updrafts to focus on activation zones. A range-resolved aerosol measurement such as lidar extinction is valuable because surface aerosol measurements may not be useful when the boundary layer is poorly mixed, or when a surface stable layer exists. Sorting by LWP removes the ambiguity in the relationship between aerosol and r_e versus that between LWP and r_e. *Kim et al.* [2003] and

Garrett et al. [2004] performed similar analyses at SGP and at the North Slope of Alaska (NSA) site, respectively, but used surface aerosol scattering as a proxy for CCN and retrieved r_e using MFRSR and MWR. Their analyses considered much longer sampling periods (months to years).

In the following we present an analysis of retrievals pertaining to the first indirect effect by calculating

$$\text{IE} = -\frac{dlnr_e}{dln\alpha}, \tag{8}$$

[*Feingold et al.*, 2001], where r_e represents a vertically-averaged (weighted by LWC) effective radius, and α is the extinction from the Raman lidar at a wavelength of 355 nm, at a prescribed altitude. Note that a positive IE indicates a decrease in drop size with increasing aerosol extinction. The calculation of IE is useful because, being a function of the relationship between N_d and N_a, it can be compared to theoretically derived values ($N_d \propto N_a^{3\times\text{IE}}$); for example, *Twomey* [1977] predicted $N_d \propto N_a^{0.7}$ or an IE of ~ 0.23. Moreover, IE is bounded and < 0.33. A further advantage of calculating the logarithmic slope is that it is a relative, rather than an absolute measure of the response of drop size to changes in aerosol.

Figure 8 shows plots of r_e vs α for three days, May 8, 13, and 17 which were deemed suitable for the analysis, having met the requirements of being single layered, nonprecipitating, boundary layer clouds. Data are plotted on the same axes to illustrate the strong differences in aerosol conditions on the three days. On May 8 aerosol loadings were abnormally high ($\alpha \sim 1.0$); May 13 and 17 had $\alpha \sim 0.3$. IE is calculated from a least-absolute-deviation fit to the points. We stress that the values of IE are independent of the assumed value of N_d used in the MMCR retrieval of r_e (section 2 (iii)) because of the definition of IE. A line with slope 0.33 and arbitrary intercept is superimposed on each plot. In each case the data are stratified by LWP to try to minimize the effect of LWP on r_e. A finer LWP binning to that used here is generally preferred [*Feingold et al.*, 2003] but this frequently results in an unreliable regression due to a dearth of data. A general separation in r_e for the three LWP

bins is clear. Note that on May 13, there is a great deal of scatter in the data and nonphysical IE > 0.33 are calculated.

Table 2 performs a similar analysis for a broader set of parameters: r_e is calculated using either the MFRSR or radar data, together with various proxies for cloud condensation nuclei; lidar extinction (355 nm) at an altitude of 350 m; surface aerosol scattering (550 nm) $\sigma_{sp,g}$; and surface aerosol number concentration N_a of particles > 0.1 μm diameter measured by a PCASP. For MMCR, the data are broken down by day, and in addition data from all three days are grouped together. When r_e is derived from MFRSR, IE has not been calculated on individual days because the 5 min temporal resolution yields too few points for reliable regression. Table 2 suggests that IE is very sensitive to the r_e retrieval method, as well as to the CCN proxy. The radar-derived r_e shows fairly consistent, and physically plausible positive IE values when aerosol extinction is used as a CCN proxy on May 8 and 17 but, as stated before, on May 13 the values can be unrealistically high. Use of N_a and $\sigma_{sp,g}$ as proxies results in highly variable and even negative IE on individual days but when the days are grouped together, results using α and $\sigma_{sp,g}$ are similar. N_a tends to be an unreliable proxy for CCN in spite of the fact that it should be the most tightly related to the aerosol population from which CCN derive. This may be due to decoupling between the surface N_a and the aerosol entering the cloud, although $\sigma_{sp,g}$ is also a surface measurement and yields a more robust IE. It may also reflect situations where the CCN derive from particles smaller than the lower size limit of the PCASP (< 0.1 μm diameter).

For the MFRSR r_e, the grouped data indicate a consistent IE of 0.36 in the highest LWP bin when either α or $\sigma_{bsp,g}$ are used. (Note that similar values are obtained by the radar-derived r_e, although at lower LWP.) At lower LWPs, IE tends to be nonphysical and highly variable. Differences in IE between MFRSR and MMCR can be due to a number of factors including differences in retrieved r_e, as well as differences in the number of data points in the regression stemming from the disparity in temporal

19

resolution. (There are roughly 15 × more data points in the MMCR analyses.) Data sets pertaining to much longer sampling periods could be used to improve MFRSR statistics [as was done by *Kim et al.,* 2003].

Regarding the radar-derived r_e, we consider whether the differences in IE among the three days (Figure 8) is a function of other aerosol physical characteristics. Calculations of the aerosol uptake of water vapor $[f(\mathrm{RH})]$ by both nephelometer and lidar [*Pahlow et al.,* 2005] suggest higher $f(\mathrm{RH})$ on May 17, whereas the highest IE is on May 13. Unfortunately, there are just too few cases from which to draw conclusions, or to consider extending this analysis to other measurements such as the Ångström exponent or single scattering albedo.

5. Discussion and Summary

This paper has examined three cloudy events during the ARM May 2003 aerosol intensive operations period. The focus has been on (i) comparison of five different methods of drop effective radius r_e retrieval for a cloud with extensive cover on May 17 2003; (ii) presentation of a general methodology for deriving a best estimate of r_e from instruments with disparate sampling volumes, footprints and spatial resolutions; and (iii) comparison of a relationship closely tied to the first aerosol indirect effect (the relationship between r_e and aerosol, as quantified by Equation 8) based on different r_e retrievals and different proxies for CCN.

On May 17 2003 a nonprecipitating cloud (radar reflectivity $\sim$ -20 dBZ) with LWP on the order of 100 g m^{-2} was sampled with a variety of instruments. The target cloud was ideal in that it was relatively homogeneous at the spatial scale of the remote sensors, and thus amenable to robust retrievals by remote sensors employing optical retrievals. The absence of drizzle made it a good target cloud for drop-size retrieval by a cloud radar. We have shown that there is good agreement (within $\sim$ 20%) between r_e retrievals from the collocated airborne spectral solar flux radiometer (SSFR), the surface-based Multi-Filter Rotating Shadowband Radiometer (MFRSR), a cloud radar (MMCR), and the satellite-borne Moderate-

Resolution Imaging Spectroradiometer (MODIS). An airborne in-situ Cloud-Aerosol-Precipitation-Spectrometer (CAPS) probe about 30 km away yielded consistent measurement of r_e, although horizontal variability in the cloud at this scale makes it difficult to make direct comparison.

A general methodology for retrieving a best estimate of r_e from a variety of remote sensors, each with different sampling characteristics, has been presented and applied to the May 17 case. The approach is based on a generalized least squares approach, i.e., minimization of a cost function consisting of the weighted squared errors. The method incorporates information on the height dependence of r_e from the radar, and temporal/spatial averages for the spectrometers and radiometers. For the case in question, the best-estimate profile of r_e is shown in Figure 7. Sensitivity of this retrieval to some of the applied weighting functions is also noted and suggests possible refinements in future studies. We suggest that methodologies of this kind should be considered when attempting to reconcile geophysical measurements made by a variety of different instruments.

Finally, on three days during the IOP, r_e retrievals from the MFRSR and cloud radar have been used in conjunction with surface aerosol measurements or vertically pointing lidar to measure the effect of aerosol on cloud drop size. It is shown that in spite of the general agreement in r_e derived from MFRSR and radar on May 17, a measure related to the first aerosol indirect effect (Equation 8) can differ quite significantly between the two methods. Three choices of CCN proxy are used: lidar extinction at a height of 350 m, surface aerosol scattering coefficient (at 550 nm), and surface aerosol accumulation mode number concentration (measured by an in-situ optical probe). It is shown that both the choice of the r_e retrieval, and the choice of proxy, strongly affect the magnitude of the drop-size response to changes in aerosol. It is suggested that more work needs to be done to determine the most suitable proxies for CCN and the most appropriate drop-size retrieval method. Unfortunately, data availability is often limited; for example, the only r_e retrieval available at night

is the radar (and MWR) retrieval. Radar retrievals are also routinely available at high temporal resolution (20 s). However, radar retrievals of r_e suffer from very high sensitivity to drop size ($\langle r^6 \rangle$-weighting) and are therefore of limited value when drizzle begins to form. At high enough sun angles, and for horizontally homogeneous clouds, radiometers such as MFRSR may be preferable, given their relative insensitivity to large drops. Alternatively, one might consider best estimate retrievals of r_e such as the one proposed here, where multiple instruments that routinely measure drop size are used to produce a more robust measure of r_e.

From the perspective of CCN proxies, different conditions may also call for different strategies. Under well-mixed conditions, surface aerosol measurements are likely to be the most useful, particularly a measure of aerosol concentration for particles greater than about 25 nm radius. During stable conditions, lidar extinction at some height beneath the cloud, where aerosol humidification effects are not significant, will be a better proxy for the aerosol entering cloud base. Refinement of these techniques is expected to yield valuable data for long-term monitoring of aerosol-cloud interactions at surface sites and to complement the global coverage of satellites.

References

Albrecht, B., Aerosols, cloud microphysics, and fractional cloudiness, *Science, 245,*

1227-1230, 1989.

Barnard J. C., J. C. Doran, S. Zhong, and C. N. Long, A comparison of cloud properties at Barrow and SHEBA during the Summer of 1998, *Proceedings of the 11-th Atmospheric Radiation Measurement (ARM) Science Team Meeting,* March 2000, Atlanta, 2001.

Baumgardner, D., H. Jonsson, W. Dawson, D. O'Connor, and R. Newton, The cloud, aerosol and precipitation spectrometer: A new instrument for cloud investigations, *Atmos. Res., 59-60,* 251–264, 2001.

Bergstrom, R.W., P. Pilewskie, B. Schmid, and P. B. Russell, Estimates of the spectral aerosol single scattering albedo and aerosol radiative effects during SAFARI 2000. *J. Geophys. Res., 108,* No. D13, 8474, doi:10.1029/2002JD002435, 2003.

Brenguier J.-L., and 9 coauthors, An overview of the ACE-2 CLOUDYCOLUMN closure experiment, *Tellus, 52B,* 815–827, 2000.

Bréon. F.-M., D. Tanré, and S. Generoso, Aerosol effect on cloud droplet size monitored from satellite, *Science, 295,* 834–838, 2002.

Cressie, N. A. C., *Statistics for Spatial Data,* revised reprint, John Wiley and Sons Inc., New York, 900 pp., 1993.

Durkee, P. A., K. K. Noone, and R. T. Bluth, The Monterey Area Ship Track Experiment, *J. Atmos. Sci., 57,* 2523–2541, 2000.

Feingold, G., L. A. Remer, J. Ramaprasad, and Y. Kaufman, Analysis of smoke impact on clouds in Brazilian biomass burning regions: An extension of Twomey's approach, *J. Geophys. Res., 106,* 22,907–22,922, 2001.

Feingold, G., W. L. Eberhard. D. E. Veron, and M. Previdi, First measurements of the Twomey aerosol indirect effect using ground-based remote sensors, *Geophys. Res. Lett., 30,* No. 6, 1287, doi:10.1029/2002GL016633, 2003.

Feingold, G., Modeling of the first indirect effect: Analysis of measurement

requirements, *Geophys. Res. Lett., 30,* 1997, doi:10.1029/2003GL017967, 2003.

Frisch, A. S., C. W. Fairall and J. B. Snider, On the measurement of stratus cloud and drizzle parameters with a K_α- band Doppler radar and a microwave radiometer, *J. Atmos. Sci., 52,* 2788–2799, 1995.

Frisch, A. S., M. Shupe, I. Djalalova, G. Feingold, and M. Poellot, The retrieval of stratus cloud droplet effective radius with cloud radars, *J. Atmos. Ocean. Technol..,, 19,* 835–842, 2002.

Garrett T. J., C. Zhao, X. Dong, G. G. Mace, P. V. Hobbs, Effects of varying aerosol regimes on low-level Arctic stratus, *Geophys. Res. Lett., 31,* doi:10.1029/2004GL019928, 2004.

Guenther, B., X. Xiong, V. V. Salomonson, W. L. Barnes and J. Young, On-orbit performance of the Earth Observing System Moderate Resolution Imaging Spectroradiometer: First year of data, *Rem. Sens. Environ., 83,* 16-30, 2002.

Han, Q., W. B. Rossow, J. Chou, and R. M. Welch, Global survey of the relationships of cloud albedo and liquid water path with droplet size using ISCCP, *J. Climate, 7,* 1516–1528, 1998.

Harrison, L., and J. Michalsky, Automated multifilter rotating shadow-band radiometer: an instrument for optical depth and radiation measurements, *Appl. Opt., 33,* 5118-5125, 1994.

Holben, B.N., T. F. Eck, I. Slutsker, D. Tanré, J. P. Buis, A. Setzer, E. Vermote, J. A. Reagan, Y. J. Kaufman, T. Nakajima, F. Lavenu, I. Jankowiak and A. Smirnov, AERONET–A federated instrument network and data archive for aerosol characterization, *Remote Sens. Environ., 66,* 1–16, 1998.

Hu, Y, X., and K. Stamnes, An accurate parameterization of the radiative properties of water clouds suitable for use in climate models, *J. Climate, 6,* 728, 1993.

Kaufman, Y. J., and T. Nakajima, Effect of Amazon smoke on cloud microphysics

and albedo – analysis from satellite imagery, *J. Appl. Meteorol., 32,* 729–744, 1993.

Kim B.-G., S. E. Schwartz, M. A. Miller, Q. Min, Effective radius of cloud droplets by ground-based remote sensing: Relationship to aerosol, *J. Geophys. Res., 108,* doi:10.1029/2003JD003721, 2003.

Leaitch, W. R., C. M. Banic, G. A. Isaac, M. D. Couture, P. S. K. Liu, I. Gultepe, and S.-M. Li, Physical and chemical observations in marine stratus during the 1993 North Atlantic Regional Experiment: Factors controlling cloud droplet number concentrations, *J. Geophys. Res., 101* , 29,123–29,135, 1996.

Liljegren, J.C, *Automatic Self-calibration of ARM Microwave Radiometers,* Microwave Radiometry and Remote Sensing of the Earth's Surface and Atmosphere, edited by P. Pampaloni and S. Paloscia, pp. 433–443, VSP Press, 1999.

Moran, K.P., B. E. Martner, D. C. Welsh, D. A. Merritt, M. J. Post, and T. Uttal, ARM's cloud-profiling radar, *Proc. of the 28th Conference on Radar Meteorology,* Austin, TX, 1997.

Min, Q.-L., and L. C. Harrison, Cloud properties derived from surface MFRSR measurements and comparison with GOES results at the ARM SGP site, *Geophys. Res. Lett., 23,* 1641–1644, 1996a.

Min, Q.-L., and L. C. Harrison, An adjoint formulation of the radiative transfer method, *J. Geophys. Res., 101,* 1635–1640, 1996b.

Min, Q.-L., and L. C. Harrison, Comparison of model-predicted total shortwave with measurements under overcast cloud conditions, *Proceedings of the Eighth ARM Science team meeting,* Tucson, 493, 1998.

Min, Q.-L., L. C. Harrison, and E. Clothiaux, Joint statistics of photon path length and cloud optical depth: case studies, *J. Geophys. Res., 106,* 7375–7386, 2001.

Min, Q.-L., M. Duan, and R. Marchand, Validation of surface retrieved cloud

optical properties with in situ measurements at the Atmospheric Radiation Measurement Program (ARM) South Great Plains site, *J. Geophys. Res., 108,* doi:10.1029/2003JD003385, 2003.

Min, Q., E. Joseph, and M. Duan, Retrievals of thin cloud optical depth from a multifilter rotating shadowband radiometer, *J. Geophys. Res., 109,* doi:10.1029/2003JD003964, 2004.

Nakajima, T., A. Higurashi, K. Kawamoto, and J. E. Penner, A possible correlation between satellite-derived cloud and aerosol microphysical parameters, *Geophys. Res. Lett., 28,* 1171–1174, 2001.

Pahlow, M., G. Feingold, A. Jefferson, E. Andrews, J. A. Ogren, J. Wang, Y.-N. Lee, and R. A. Ferrare, Comparison between lidar and nephelometer measurements of aerosol hygroscopicity at the Southern Great Plains Atmospheric Radiation Measurement site, *J. Geophys. Res.,* submitted, (this issue).

Pilewskie, P., J. Pommier, R. Bergstrom, W. Gore, S. Howard, M. Rabbette, B. Schmid, P. V. Hobbs, and S. C. Tsay, Solar spectral radiative forcing during the Southern African Regional Science Initiative. *J. Geophys. Res., 108,* No. D13, 8486, doi:10.1029/2002JD002411, 2003.

Platnick, S., Vertical photon transport in cloud remote sensing problems, *J. Geophys. Res., 105,* 22,919–22,935, 2000.

Platnick, S., M.D. King, S. A. Ackerman, W. P. Menzel, B. Baum, J. Ridi and R. Frey, The MODIS cloud products: Algorithms and examples from Terra, *IEEE Trans. Geosci. Remote Sens., 41,* 459-473, 2003.

Ramanathan, V., and 39 coauthors, Indian Ocean Experiment: An integrated analysis of the climate forcing and effects of the great Indio-Asian haze. *J. Geophys. Res., 106,* No. D22, 28,371–28,398, 2001.

Rosenfeld, D. and I. M. Lensky, Satellite-based insights into precipitation formation processes in continental and maritime convective clouds., *Bull. Am. Meteorol.*

Soc., 79, 2457–2476, 1998.

Rosenfeld, D., and G. Feingold, Explanation of the discrepancies among satellite observations of the aerosol indirect effects. *Geophys. Res. Lett.,* No. 14, 1776, doi:10.1029/2003GL017684, 2003.

Schwartz, S. E., Harshvardhan, and C. M. Benkovitz, Influence of anthropogenic aerosol on cloud optical properties and albedo shown by satellite measurements and chemical transport modeling. *Proceedings Natl. Acad. Sci., 99,* 1784–1789, 2002.

Twomey, S., Pollution and the planetary albedo, *Atmos. Environ., 8,* 1251–1256, 1974.

Twomey, S., The influence of pollution on the shortwave albedo of clouds, *J. Atmos. Sci., 34,* 1149–1152, 1977.

Twomey, S., and T. Cocks, Remote sensing of cloud parameters from spectral reflectance in the near-infrared, *Cont. Atmos. Phys., 62,* 172, 1989.

Warner, J., A reduction in rainfall associated with smoke from sugar-cane fires: An inadvertent weather modification? *J. Appl. Meteorol., 7,* 247–251, 1968.

Appendix

We summarize the role of the weighting functions and the construction of the design matrix **M** and the covariance matrix $\boldsymbol{\Sigma}$ used for the weighted least squares problem illustrated in Section 3.2.3.

Weighting functions: As an illustration, we use an exponential weighting function for MODIS and SSFR retrievals and a constant weighting throughout the cloud column for MFRSR retrievals. Whereas the latter is a reasonable approximation, the former does not represent a penetration depth of multiply scattered photons *Platnick* [2000]. Retrievals of r_e from multiple instruments, such as MMCR or MFRSR in combination with MWR, require consideration of more complex weighting functions that take into account the vertical response of both instruments. Such investigation is beyond the scope of the current paper.

We note that equations of the form of (5) allow one to represent the weighting function in the least squares problem as the $h^{1/3}$ weighted center-of-mass but the exact form of the function does not enter the least squares solution. For MODIS and SSFR, the quantity given by (5) decreases as the decay rate of the exponential weight decreases. To illustrate the effect of the decay rate we test two extreme values, 1/17 m and 1/340 m, which we believe bound the potential effects of the weighting on the retrieval. Similar arguments with respect to insensitivity to the exact form of the weighting function apply to MFRSR+MWR and MMCR+MWR retrievals, but as noted we defer sensitivity studies of this kind to future work.

Design matrix M: The first column contains ones, the entries in the second column depends on the measurement device. The weighting function for MODIS and SSFR have an exponential decay with rate 1/17 m or 1/340 m. Table 3 summarizes the entries. For MODIS and SSFR the integrals were calculated numerically.

Covariance matrix $\boldsymbol{\Sigma}$: As mentioned above, we do not model the retrieval

error process and the process $\mathcal{Z}$ separately. However, it is reasonable to assume that both processes are independent. Then $\mathbf{\Sigma}$ is simply the sum of the covariance of the retrieval error and the covariance of the spatial process which are described below.

First we address the covariance associated with the retrieval errors. We assume that all the measurement errors and thus the retrieval errors are uncorrelated. Therefore, the covariance matrix has only non-zero elements on its diagonal with values related to the retrieval errors as given in Table 1. This assumption can be justified as follows. Since we have different retrieval techniques and fundamentally different measurement devices there is no physical reason for correlations between the different devices. Assuming a homogeneous cloud, heuristic techniques can be used to justify that the MODIS data do not exhibit any spatial structure. As mentioned, the SSFR data was thinned to eliminate any correlation. Even if the MMCR were to have any correlations between retrieval errors it would be modelled by the correlation of the process $\mathcal{Z}$ (see below).

Consider now the covariance associated with the process $\mathcal{Z}$. We first partition $\mathbf{\Sigma}$ into 4×4 sub-matrices of different sizes according to the different measurement devices. For example, the first sub-matrix is associated with MMCR and has size 688×688. We use the high resolution MMCR data to examine the spatio-temporal structure of the process. We essentially estimate a spatio-temporal variogram, defined as follows

$$2\gamma(|h_i - h_j|, |t_i - t_j|) = \mathrm{Var}(R(h_i, t_i) - R(h_j, t_i)) \tag{A1}$$

where $R(x_i)$ is the MMCR retrieval at height h_i and time t_i. The empirical form of the variogram is used to estimate the correlation structure in time and space. For a detailed discussion on estimating and fitting dependence structures in correlated data, the reader is referred to *Cressie* [1993]. An exponential correlation structure with marginal rates of 1/200 m and 1/100 s describes the empirical structure sufficiently well. To determine the correlation at lower

resolutions (MODIS, SSFR, MFRSR) the variogram is simply integrated over the respective spatial and temporal domain. Since the covariances in the MODIS, SSFR, MFRSR blocks and all off-diagonal blocks are one to two orders of magnitude smaller than the retrieval errors, we set all these values to zero.

Table Captions

Table 1.   Summary of various instruments, their sampling characteristics, and approximate errors in r_e retrieval. $\langle r^n \rangle$ denotes the nth moment of the drop size distribution $n(r)$.

Table 2. Values of IE (Equation 8) derived from r_e measured by either MFRSR or MMCR, and from aerosol proxies that include Raman lidar aerosol extinction (wavelength 355 nm; height = 350 m), surface aerosol scattering $\sigma_{sp,g}$ (measured by a nephelometer at 550 nm), or surface aerosol concentration N_a measured by a PCASP. For MFRSR, data from all 3 days are grouped together to improve statistics. Data for N_a were not available on May 8. Note that negative values of IE are nonphysical and suggest an increase in r_e with increasing aerosol amount. IE should be bounded by 0 and 0.33.

Table 3. Entries of the second column of the matrix **M** for the 706 data points. The numerical values are based on $h_{top} = 1350$ m and $h_{bot} = 675$ m for cloud top and cloud bottom (height above ground level). "MFRSR" indicates r_e retrieval from MFRSR and MWR. "MMCR" indicates r_e retrieval from MMCR and MWR.

Figure Captions

Figure 1. Aqua satellite image of the synoptic scale cloud cover on May 17 2003 at 18:45 UTC.

Figure 2. (a) Time-height cross-section of radar reflectivity from the MMCR at SGP on May 17; (b) Time series of LWP measured by the microwave radiometer.

Figure 3. Time series of CIRPAS Twin Otter airborne measurements of (a) N_d, (b) LWC, and (c) r_e by the CAPS instrument.

Figure 4. Time series of r_e measured by SSFR on board the CIRPAS Twin Otter aircraft. The time of overflight of the SGP ground site is indicated by the vertical dotted line.

Figure 5. Time series of r_e derived from the surface-based MFRSR and MMCR at

SGP. The time of the Twin Otter aircraft overflight is marked by a vertical dotted line.

Figure 6. Spatial depiction of the MODIS-derived r_e during overpass of SGP. The individual pixels correspond to 2 km $\times$ 4.8 km boxes in the region of SGP. (Boxes are not exactly to scale.) The central box is the closest to SGP. Colors correspond to the value of r_e as indicated by the scale.

Figure 7. Measurements from May 17 2003 used in the best-estimate retrieval of drop size according to model Equation (2). The red line represents the best estimate of r_e with decay rate 1/17 m. The dotted line is for decay rate 1/340 m. Other line types are as indicated.

Figure 8. r_e measured by MMCR and MWR plotted vs. aerosol extinction α as measured by the Raman lidar (at a height of 350 m) for May 8, 13, and 17. Data are sorted by three fairly broad LWP bands. Values of IE are based on Equation (8) and indicate the relative change in r_e for a relative change in extinction. The solid line has a slope of 0.33 and indicates the theoretical upper limit of IE. Correlation coefficients between $\ln(r_e)$ and $\ln(\alpha)$ are calculated in each of the LWP bands 50–75 g m^{-2}, 75–113 g m^{-2}, 113–169 g m^{-2}. For May 8, they are respectively, for each of the LWP bands: -0.05, -0.15, -0.24; May 13: -0.73, -0.51, -0.25; May 17: -0.28, -0.42, -0.29.

	Parameter			
	Sampling Time, s	Sampling Volume/ Footprint	weighting	$\sim$ error in r_e, %
MFRSR	300	Circle radius = 1 km	$\langle r^3 \rangle; \langle r^2 \rangle$	13
MMCR	20	700 m^3	$\langle r^6 \rangle; \langle r^3 \rangle$	15 - 20
SSFR	1	Circle radius = 2.7 km	$\langle r^3 \rangle; \langle r^2 \rangle$	15 - 20
MODIS	10^{-4}	2 km $\times$ 4.8 km	$\langle r^3 \rangle; \langle r^2 \rangle$	10
CAPS	1	7 cm^3	$n(r)$	15 - 20

Table 1. Summary of various instruments, their sampling characteristics, and approximate errors in r_e retrieval. $\langle r^n \rangle$ denotes the nth moment of the drop size distribution $n(r)$.

			LWP g m^{-2}		
			50-75	75-113	113-169
MFRSR	r_e, α	All	1.07	-0.39	0.36
	r_e, $\sigma_{sp,g}$	All	-0.38	-0.23	0.36
	r_e, N_a	All	0.85	0.03	0.003
MMCR	r_e, α	All	0.39	0.39	0.16
		May 8	0.01	0.09	0.06
		May 13	0.70	0.68	0.33
		May 17	0.22	0.33	0.19
	r_e, $\sigma_{sp,g}$	All	0.34	0.26	0.14
		May 8	0.03	-0.02	0.03
		May 13	-0.05	-0.16	0.10
		May 17	0.11	-0.16	-0.24
	r_e, N_a	All	0.94	0.80	1.55
		May 8	-	-	-
		May 13	-1.17	-2.40	-1.06
		May 17	0.05	0.22	0.36

Table 2. Values of IE (Equation 8) derived from r_e measured by either MFRSR or MMCR, and from aerosol proxies that include Raman lidar aerosol extinction (wavelength 355 nm; height = 350 m), surface aerosol scattering $\sigma_{sp,g}$ (measured by a nephelometer at 550 nm), or surface aerosol concentration N_a measured by a PCASP. For MFRSR, data from all 3 days are grouped together to improve statistics. Data for N_a were not available on May 8. Note that negative values of IE are non physical and suggest an increase in r_e with increasing aerosol amount. IE should be bounded by 0 and 0.33.

	Data points	Weight function	Entry
MMCR	688	—	$h^{1/3} \in [8.77, 11.05]$
MFRSR	6	const.	$\frac{3}{4(h_{top} - h_{bot})}(h_{top}^{4/3} - h_{bot}^{4/3}) = 9.95$
MODIS	9	$\exp(-\mathrm{rate}(h_{top} - h))$	11.01 for rate 1/17 m and
			10.35 for rate 1/340 m
SSFR	3	$\exp(-\mathrm{rate}(h_{top} - h))$	11.01 for rate 1/17 m and
			10.35 for rate 1/340 m

Table 3. Entries of the second column of the matrix $\mathbf{M}$ for the 706 data points. The numerical values are based on $h_{top} = 1350$ m and $h_{bot} = 675$ m for cloud top and cloud bottom (height above ground level). "MFRSR" indicates r_e retrieval from MFRSR and MWR. "MMCR" indicates r_e retrieval from MMCR and MWR.

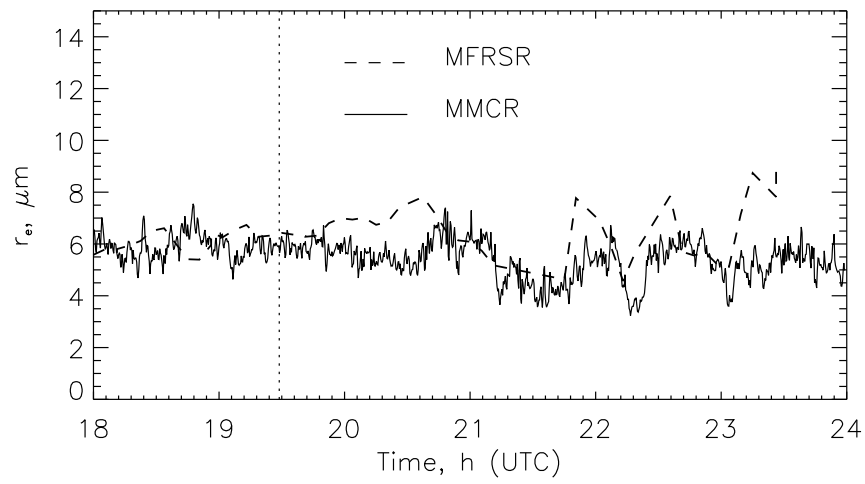MYD021KM.A2003137.1845.004.2004091193540.hdf
Aqua MODIS Truecolor Scene
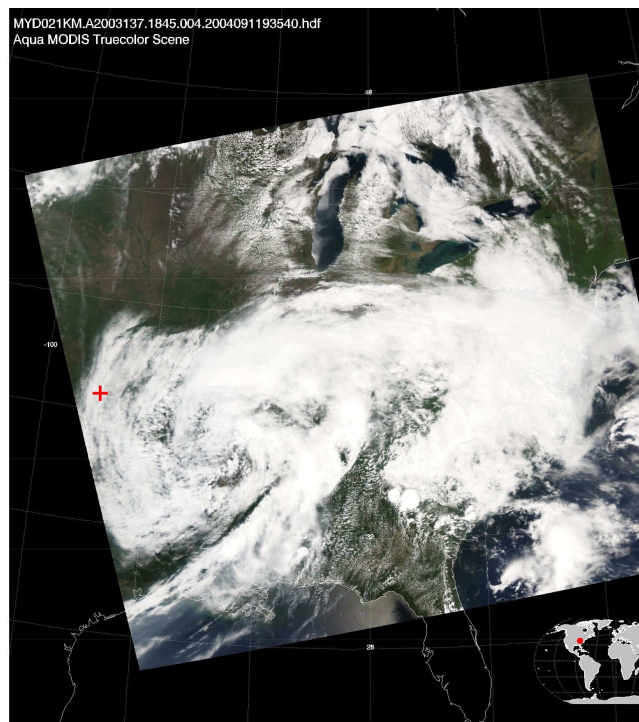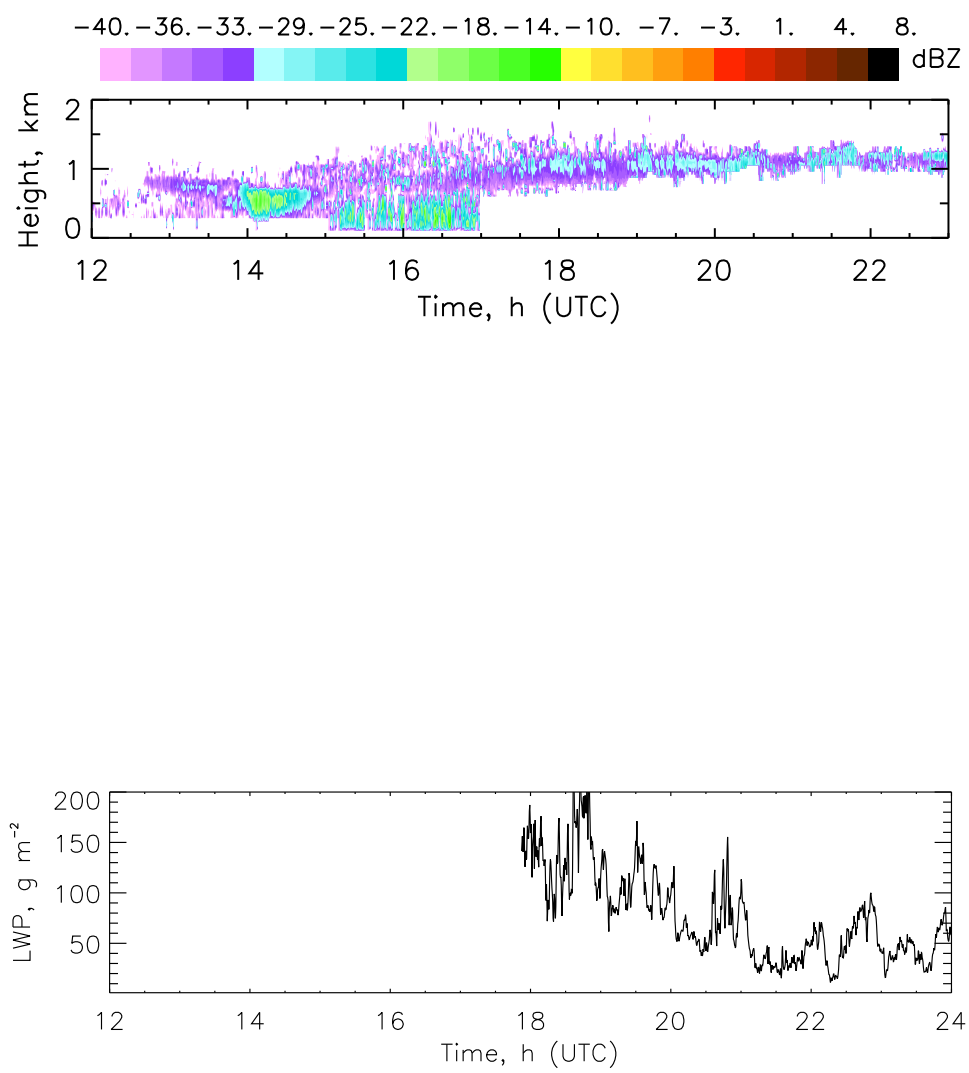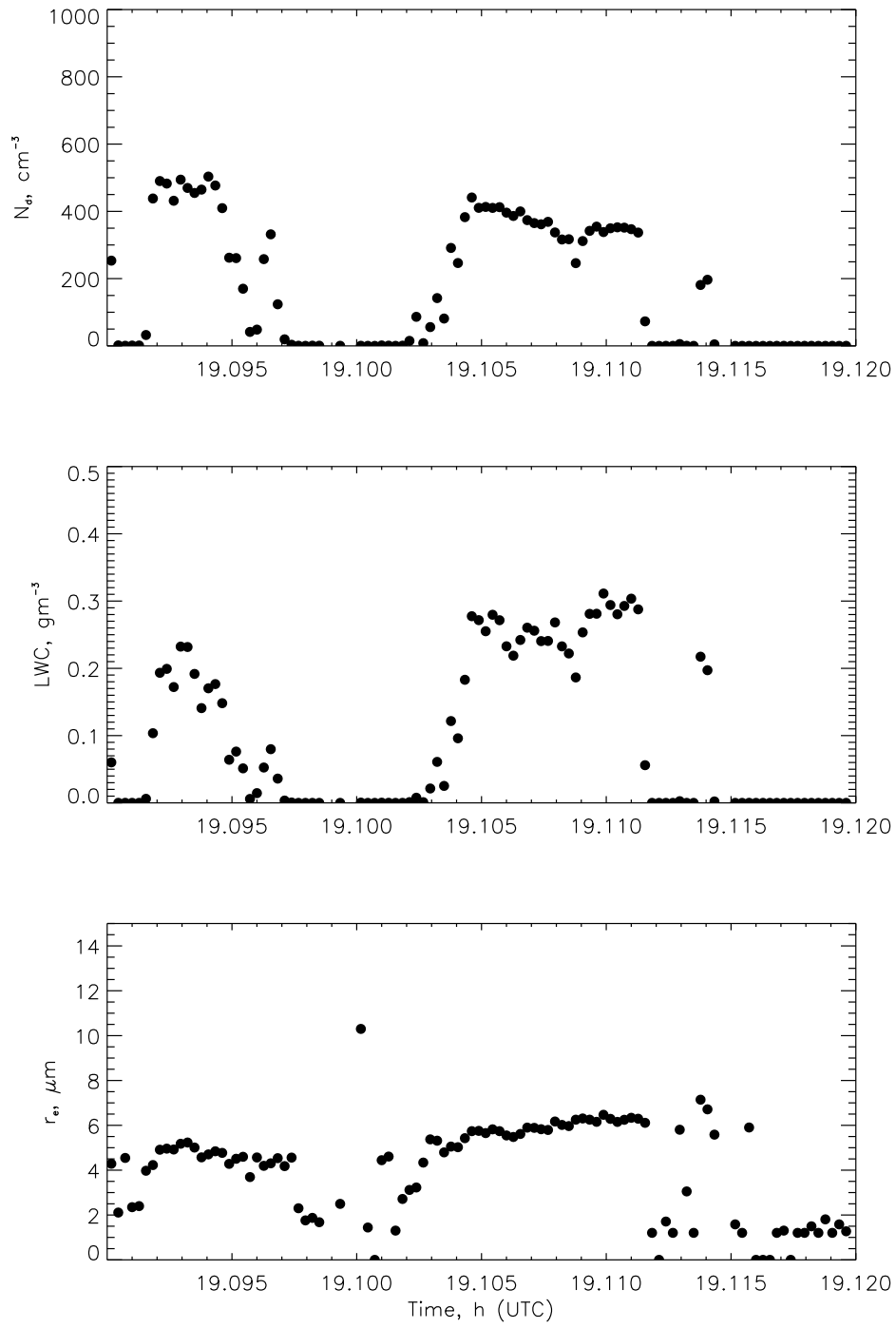
Figure 1

Figure 2

Figure 3
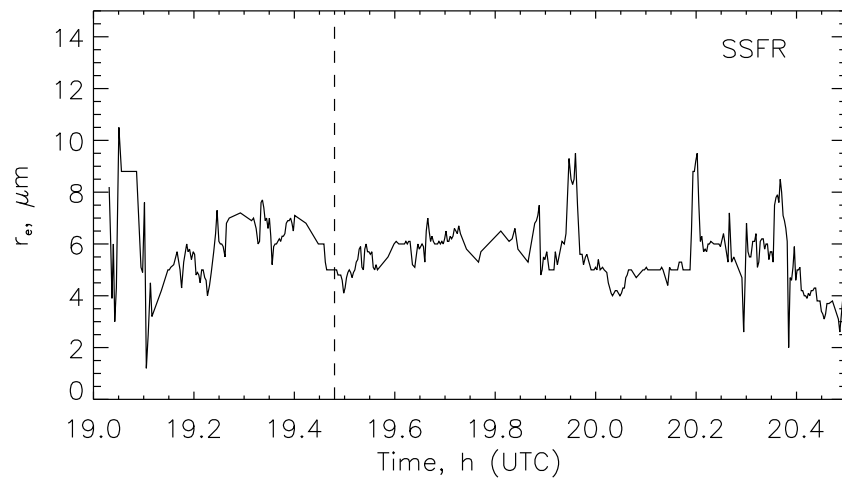
Figure 4

Figure 5
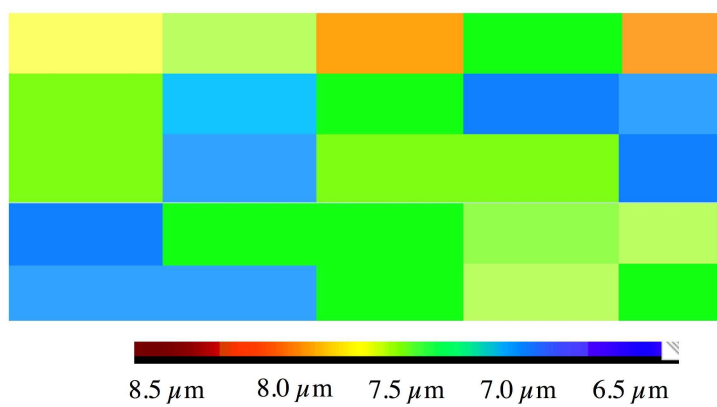
Figure 6

Figure 7

Figure 8